PHYSICAL REVIEW D **94,** 075009 (2016)

Monotop signature from the supersymmetric $t\bar{t}H$ channel

Dorival Gonçalves,[1] Kazuki Sakurai,[1] and Michihisa Takeuchi[2]

[1]*Institute for Particle Physics Phenomenology, Department of Physics, Durham University, Durham DH1 3LE, United Kingdom*

[2]*Kavli IPMU (WPI), UTIAS, University of Tokyo, Kashiwa 277-8583, Japan*

(Received 22 June 2016; published 19 October 2016)

We point out that a distinctive monotop signature is present in natural supersymmetry scenarios when a scalar top quark and Higgsinos are almost mass degenerate. This signature originates from a supersymmetric counterpart of the $t\bar{t}H$ process, i.e. $pp \to \tilde{t}t\tilde{h}$. Unlike monojet signatures exploiting initial state radiation, this channel can be regarded as a clear signature of a light stop and Higgsinos, allowing a direct probe of the stop and neutralino sectors. The production rate of this channel largely depends on the up-type Higgsino components in the neutralinos while the stop sector is sensitive to angular distributions of the top-quark's decay products. We develop an optimal search strategy to capture the supersymmetric $t\bar{t}H$ process and find that a high luminosity LHC can probe the stop and Higgsino sectors with $m_{\tilde{t}_1} \lesssim 380$ GeV and $m_{\tilde{t}_1} - m_{\tilde{\chi}_1^0} \lesssim m_W$. Additionally, we propose a kinematic variable with which one can measure the stop mixing in this channel.

DOI: 10.1103/PhysRevD.94.075009

I. INTRODUCTION

After the long shutdown CERN's Large Hadron Collider (LHC) has resumed colliding protons, almost doubling the collision energy to 13 TeV. With this highest-ever energy, the LHC Run 2 expects to observe the processes with multiple heavy particles such as $t\bar{t}H$ [1–10], tqH [11–16], and possibly HH [17–27]. Observing these processes is not only interesting by its own right but also crucial to directly measure the interaction of the Higgs boson with top quarks and the Higgs boson itself.

Another compelling physics target of Run 2 is searches for new physics beyond the Standard Model. The leading candidate of such models is supersymmetry (SUSY), in which the gauge hierarchy problem is elegantly solved due to the underlying symmetry between bosons and fermions. In the minimal SUSY Standard Model the bare Higgs mass-squared parameter and the radiative correction to it are given by the mass scales of Higgsinos and scalar top quarks (stops), respectively. *Naturalness*, therefore, requires Higgsinos and stops not to be significantly heavier than the gauge boson mass scale, while it leaves the rest of the spectrum rather unconstrained.[1] Indeed, naturalness remains almost intact even if all other SUSY particles are pushed up to a few TeV, significantly heavier than their exclusion limit obtained in the Run 1 and early 13 TeV data collected in 2015. Such a scenario, called *Natural SUSY*, has been extensively studied in the literature [28–58].

Reflecting its importance and nontriviality [59–72], numerous ATLAS and CMS analyses have been devoted to light stop searches. The exclusion limit on the mass of the lighter stop, $\tilde{t}_1$, largely depends on its decay modes. In Natural SUSY lighter neutralinos ($\tilde{\chi}_1^0$ and $\tilde{\chi}_2^0$) and the lighter charginos ($\tilde{\chi}_1^\pm$) are Higgsino-like and almost mass degenerate: $m_{\tilde{\chi}_1^0} \simeq m_{\tilde{\chi}_2^0} \simeq m_{\tilde{\chi}_1^\pm}$. If $\tilde{t}_1 \to t\tilde{\chi}_1^0$ is kinematically forbidden ($m_{\tilde{t}_1} < m_{\tilde{\chi}_1^0} + m_t$), the decay mode of $\tilde{t}_1$ is dominated by

$$\tilde{t}_1 \to b\chi_1^\pm. \tag{1}$$

Because of the mass degeneracy between $\tilde{\chi}_1^\pm$ and $\tilde{\chi}_1^0$, the subsequent decay $\tilde{\chi}_1^\pm \to f\bar{f}\tilde{\chi}_1^0$ would not be observable. ATLAS and CMS have searched for this process in the di-b-jet channel [73–75]. Currently, the most stringent bound, $m_{\tilde{t}_1} \gtrsim 840$ GeV for $m_{\tilde{\chi}_1^0} \lesssim 200$ GeV, comes from the 13 TeV ATLAS analysis [75] with the integrated luminosity of 3.2 fb^{-1}. However, this limit diminishes if the mass difference $\Delta m_{\tilde{t}_1-\tilde{\chi}_1^0} \equiv m_{\tilde{t}_1} - m_{\tilde{\chi}_1^0}$ gets compressed, because the b quarks from the stop decays become soft and undetectable. For instance, it becomes as weak as $m_{\tilde{t}_1} \gtrsim 300$ GeV if $\Delta m_{\tilde{t}_1-\tilde{\chi}_1^0} \lesssim 50$ GeV.

The compressed stop-Higgsino region can be searched for by exploiting the stop pair production associated with hard QCD initial state radiation (ISR). In such events the system of two stops is boosted recoiling against the high p_T ISR jets, leading to a monojet signature as shown in the left panel of Fig. 1. Although the monojet channel is useful for discovery, it has some disadvantages.

[1]Except for gluinos. The gluinos contribute to the radiative corrections to the Higgs mass-squared parameter through renormalization group evolution of the stop mass. Since the sensitivity of the gluino mass to naturalness is higher order compared to that of stops and Higgsinos, in this paper we focus only on light stops and Higgsinos.

(i) Since it requires at least one high p_T QCD jet, the cross section is suppressed by the QCD coupling, $\alpha_s(\mu)$, approximately at the scale of the p_T cut, $\gtrsim\mathcal{O}(100)$ GeV.

(ii) There is a largeCD dijet background where one of the jets is badly mismeasured. Because of this and the above reason, the limit obtained from the monojet channel is rather weak: $m_{\tilde{t}_1} \gtrsim 320$ GeV for $\Delta m_{\tilde{t}_1-\tilde{\chi}^0_1} \lesssim 15$ GeV [74,76,77]. The limit deteriorates if the mass difference increases since the b quark from the $\tilde{t}_1 \to b\tilde{\chi}^{\pm}_1$ decay starts to be visible. For example, the limit is weakened to $m_{\tilde{t}_1} \gtrsim 200$ GeV for $\Delta m_{\tilde{t}_1-\tilde{\chi}^0_1} \gtrsim 50$ GeV [74,76,77].

(iii) The signal is entirely controlled by QCD interactions; hence the available information is limited. For example, even in the presence of an excess, it would be very difficult to find out what types of particles are produced and how they decay as we would only observe the jets from QCD radiation.

In this paper we point out that a large collision energy of 13 TeV LHC opens up the possibility of observing the stop-top-Higgsino production process, $pp \to \tilde{t}_1 t\tilde{\chi}^0_{1(2)}$,[2] providing an additional handle for the compressed stop-Higgsino region in Natural SUSY. This process is nothing but a supersymmetric counterpart of the $t\bar{t}H$ process, and analogous to the $t\bar{t}H$ it is crucial to directly probe the interaction between stops and Higgsinos. Because the stop is essentially invisible as its decay products are too soft to be observed in the compressed region, the process leads to a distinctive monotop signature as depicted in the right panel of Fig. 1. The monotop signature has been actively studied mainly in the context of the flavor violating models [79–86]. The process discussed in this paper, however, does not belong to this type since the monotop nature emerges due to the kinematics of the stop's decay products. In contrast to the monojet channel, this process has the following advantages:

(i) Despite a large mass of the system, the production rate is not too small because the stop-top-Higgsino interaction is proportional to the top Yukawa coupling, Y_t.

(ii) The QCD multijet background can be controlled by requiring an isolated lepton from top-quark decays.

(iii) The process contains rich information on the stop and neutralino sectors. For example, as will be shown in the next section, the production cross section depends dominantly on the up-type Higgsino components in the neutralinos.[3] On the other hand, the structure of the stop mixing can be probed by looking at the kinematic distributions of the b jet and the lepton from the top-quark decay as we will see in Sec. IV.

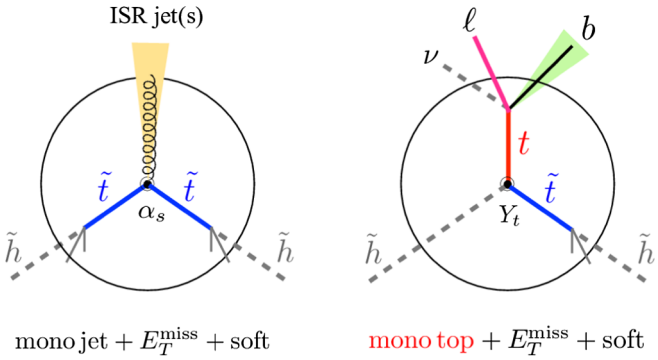

FIG. 1. Monojet event topologies channel from $\tilde{t}_1$ pair production (left) and monotop from supersymmetric $t\bar{t}H$ process (right). The grey dashed lines represent invisible particles, while the thin grey lines represent particles that are too soft to be observed. The strong coupling and the top Yukawa coupling are denoted as α_s and Y_t, respectively.

Despite the first two points, we will see that the sensitivity of the monotop channel is not greater than the conventional monojet channel. Hence the monotop may not be useful as a discovery channel. However, as we will see in Secs. III and IV, it can be used to probe the Higgsino components of the neutralino sector and the left-right handed mixing of the stop sector. On the other hand, this information is not accessible in the conventional monojet search alone.

The paper is organized as follows. In the next section, we study the production cross section of the supersymmetric $t\bar{t}H$ process and discuss how the cross section *does* and *does not* depend on the neutralino and the stop sectors. In Sec. III, an optimal search strategy is proposed based on various kinematic distributions of the signal and background. We derive the 2-σ sensitivity assuming 13 TeV LHC with 3 ab^{-1} of the integrated luminosity. In Sec. IV, we demonstrate how the stop mixing parameter can be probed by looking at the kinematic distributions of the top-quark decay products. We conclude this paper in Sec. V.

II. CROSS SECTION OF THE SUPERSYMMETRIC $t\bar{t}H$ PROCESS

Figure 2 shows some of the tree-level diagrams contributing to the supersymmetric $t\bar{t}H$ process, i.e. $pp \to \tilde{t}_1 t\tilde{\chi}^0_i$ ($i \in \{1,2\}$). As mentioned in the previous section, in Natural SUSY scenarios $\tilde{\chi}^0_1$ and $\tilde{\chi}^0_2$ are Higgsino-like and almost mass degenerate. Therefore, both $\tilde{t}_1 t\tilde{\chi}^0_1$ and $\tilde{t}_1 t\tilde{\chi}^0_2$ processes contribute to the signal. In this paper, we focus on the compressed stop-Higgsino region, in particular $m_{\tilde{t}_1} < m_{\tilde{\chi}_1} + m_W$, since searches for light stops in this

[2]This process was first studied in [78]. We consider both $\tilde{t}^*_1 t\tilde{\chi}^0_i$ and $\tilde{t}_1 \bar{t}\tilde{\chi}^0_i$ but simply write $\tilde{t}_1 t\tilde{\chi}^0_i$.

[3]The details of the neutralino sector may also be probed via the $pp \to \tilde{q}\tilde{\chi}^0_1$ process if squarks are light and $\tilde{\chi}^0_1$ is gauginolike [87,88].

parameter regime are experimentally challenging. It is worthwhile to note that if the mass difference is larger than m_t, the supersymmetric $t\bar{t}H$ process cannot easily be distinguished from the $\tilde{t}_1$ pair production where one of the stops decays into t and $\tilde{\chi}^0_{1(2)}$. The compressed stop-Higgsino region studied in this paper does not have such a complication. As can be seen in Fig. 2, the amplitude is proportional to the stop-top-neutralino vertex depicted by the red dots, and one can probe the stop and neutralino sectors through this interaction.

Before going into the details, we define the stop mixing as

$$\begin{pmatrix} \tilde{t}_1 \\ \tilde{t}_2 \end{pmatrix} = \begin{pmatrix} \cos\theta_{\tilde{t}} & \sin\theta_{\tilde{t}} \\ -\sin\theta_{\tilde{t}} & \cos\theta_{\tilde{t}} \end{pmatrix} \begin{pmatrix} \tilde{t}_R \\ \tilde{t}_L \end{pmatrix} \tag{2}$$

with $m_{\tilde{t}_1} \leq m_{\tilde{t}_2}$. The neutralino mass matrix is given by

$$M_\psi = \begin{pmatrix} M_1 & 0 & -\cos\beta\sin\theta_W m_Z & \sin\beta\sin\theta_W m_Z \\ 0 & M_2 & \cos\beta\cos\theta_W m_Z & -\sin\beta\cos\theta_W m_Z \\ -\cos\beta\sin\theta_W m_Z & \cos\beta\cos\theta_W m_Z & 0 & -\mu \\ \sin\beta\sin\theta_W m_Z & -\sin\beta\cos\theta_W m_Z & -\mu & 0 \end{pmatrix} \tag{3}$$

in the basis of $\psi_a = (\tilde{B}, \tilde{W}^0, \tilde{h}^0_d, \tilde{h}^0_u)$, where $\tan\beta$ is the ratio of the vacuum expectation values of the up- and down-type Higgs fields and θ_W is the weak mixing angle. The mass matrix is diagonalized as $NM_\psi N^T = \mathrm{diag}(m_{\tilde{\chi}^0_1}, m_{\tilde{\chi}^0_2}, m_{\tilde{\chi}^0_3}, m_{\tilde{\chi}^0_4})$ with $|m_{\tilde{\chi}^0_i}| \leq |m_{\tilde{\chi}^0_j}|$ for $i < j$, and $\tilde{\chi}^0_i = N_{ia}\psi_a$. If the electroweak gauginos are decoupled, the lighter two neutralinos become purely Higgsino-like (pure Higgsino limit) and the relevant components of the mixing matrix can be written as

$$\begin{pmatrix} N_{13} & N_{14} \\ N_{23} & N_{24} \end{pmatrix} = \begin{pmatrix} \frac{1}{\sqrt{2}} & \frac{-1}{\sqrt{2}} \\ \frac{i}{\sqrt{2}} & \frac{i}{\sqrt{2}} \end{pmatrix}. \tag{4}$$

The stop-top-neutralino interaction is given by

$$\begin{aligned} \mathcal{L} \supset -\frac{g}{\sqrt{2}}\tilde{t}_1^* \sum_i \bar{\tilde{\chi}}^0_i [(D_h^* \sin\theta_{\tilde{t}} + D_B \cos\theta_{\tilde{t}})P_R \\ + (D_h \cos\theta_{\tilde{t}} + D_{WB}^* \sin\theta_{\tilde{t}})P_L]t + \mathrm{H.c.} \end{aligned} \tag{5}$$

with

$$D_h \equiv \frac{m_t}{m_W \sin\beta} N_{i4}, \qquad D_B \equiv -2Q_u \tan\theta_W N_{i1},$$
$$D_{WB} \equiv N_{i2} + (2Q_u - 1)N_{i1}\tan\theta_W, \tag{6}$$

where $P_{R(L)} = \frac{1\pm\gamma_5}{2}$ is the chirality projection operator and $Q_u = 2/3$ is the electric charge of the top quark.

In order to parametrize the deviation from the pure Higgsino limit, we define *Higgsino measure* $\mathcal{R}$ as

$$\mathcal{R} \equiv \sigma/\sigma_{\tilde{h}}, \tag{7}$$

where σ is the total cross section of the $\tilde{t}_1 t\tilde{\chi}^0_1$ and $\tilde{t}_1 t\tilde{\chi}^0_2$ processes in the model and $\sigma_{\tilde{h}}$ is that for the pure Higgsino limit with $\tilde{t}_1 = \tilde{t}_R$ and $\sin\beta \simeq 1$. In the regime where $\tilde{\chi}^0_{1(2)}$ are Higgsino-like ($|N_{i4}| \gg |N_{i1}|, |N_{i2}|$ for $i \in \{1, 2\}$) we find approximately

$$\mathcal{R} \simeq \frac{|N_{14}|^2 + |N_{24}|^2}{\sin^2\beta}. \tag{8}$$

Within this approximation the cross section is independent of the stop mixing (we will confirm this numerically in Sec. III B) and depends dominantly on the up-type Higgsino components in $\tilde{\chi}^0_1$ (N_{14}) and $\tilde{\chi}^0_2$ (N_{24}) up to the $1/\sin^2\beta$ factor.[4]

Equation (8) has an important implication. In the compressed stop-Higgsino region ($m_{\tilde{t}_1} \simeq m_{\tilde{\chi}_2} \simeq m_{\tilde{\chi}_1}$) the monotop signal rate is determined by $m_{\tilde{t}_1}$ and $\mathcal{R}$, while the monojet signal rate is fixed only by $m_{\tilde{t}_1}$. Hence, *measuring both monojet and monotop signal rates allows us to*

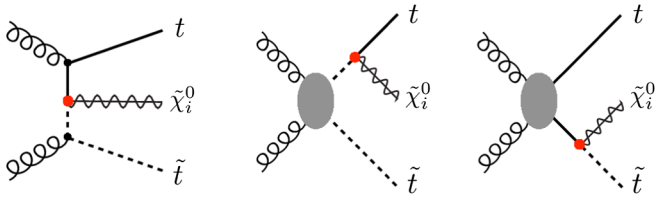

FIG. 2. Representative Feynman diagrams for the supersymmetric $t\bar{t}H$ process. The $q\bar{q}$ initial states are also possible for the latter two diagrams. The red dots denote the stop-top-Higgsino interaction. The stop propagator in the second diagram has to be far off shell in our parameter region $m_{\tilde{t}_1} - m_{\tilde{\chi}^0_1} < m_W$; hence it is clearly separated from the stop pair production.

[4]This factor is never significant unless $\tan\beta$ is extremely small. For instance $\sin^2\beta = 0.9$, 0.8, and 0.5 for $\tan\beta = 3$, 2, and 1, respectively. Moreover, small $\tan\beta$ is not favored in Natural SUSY scenarios since realizing $m_h \simeq 125$ GeV becomes even more challenging with light stops.

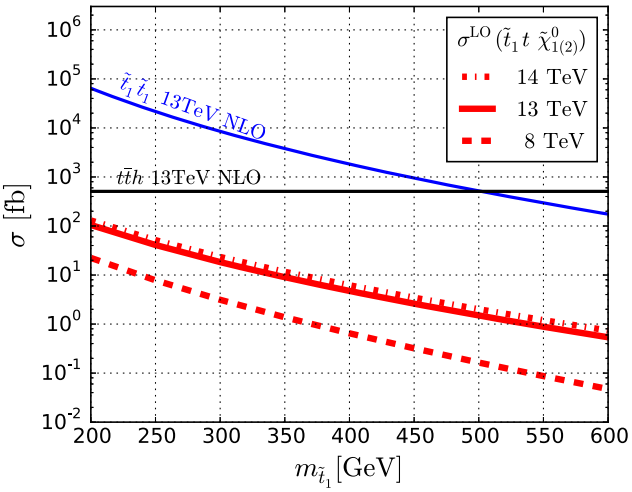

FIG. 3. LO cross section of the supersymmetric $t\bar{t}H$ process ($pp \to \tilde{t}_1 t\tilde{\chi}^0_1$ and $\tilde{t}_1 t\tilde{\chi}^0_2$ are combined) in the pure Higgsino limit at the 8 (red dashed line), 13 (red solid line), and 14 TeV (red dash-dotted line) LHC. The parameters are fixed as $\Delta m_{\tilde{t}_1-\tilde{\chi}^0_1} = 10$ GeV, $m_{\tilde{\chi}^0_2} = m_{\tilde{\chi}^0_1} + 5$ GeV, $\cos\theta_{\tilde{t}} = 1$, and $\tan\beta = 20$. These LO cross sections are compared with the NLO cross sections of the $\tilde{t}_1$ pair production (blue solid line) and the Standard Model $t\bar{t}H$ production (black solid line) at the 13 TeV LHC.

determine $\mathcal{R}$, enabling us to directly probe the neutralino sector independently of the details of the stop sector.

The red curves in Fig. 3 show the leading order (LO) cross sections of the $\tilde{t}_1 t\tilde{\chi}^0_i$ production ($i = 1$ and 2 are combined) at the 8 (dashed line), 13 (solid line), and 14 TeV (dash-dotted line) LHC in the pure Higgsino limit, i.e. $\mathcal{R} \simeq 1$. We fix $\Delta m_{\tilde{t}_1-\tilde{\chi}^0_1} = 10$ GeV, $m_{\tilde{\chi}^0_2} = m_{\tilde{\chi}^0_1} + 5$ GeV, $\cos\theta_{\tilde{t}} = 1$, and $\tan\beta = 20$ in the calculation. We use MadGraph 5 [89] to compute the cross section. The 13 TeV cross section varies from 105 to 0.53 fb as $m_{\tilde{t}_1}$ increases from 200 to 600 GeV. The ratio between the 13 and 8 TeV cross sections ($\sigma_{13\text{ TeV}}/\sigma_{8\text{ TeV}}$) is about 5 (10) for $m_{\tilde{t}_1} = 200$ (600) GeV. The 14 TeV cross section is not larger than 1.5 times the 13 TeV cross section in the range of the plot.

The LO cross section of the supersymmetric $t\bar{t}H$ process is compared with the next-to-leading order (NLO) cross sections of the $\tilde{t}_1$ pair production (blue solid line) [90–94] and the Standard Model $t\bar{t}H$ production (black solid) [95] at the 13 TeV LHC. The NLO cross section of the $\tilde{t}_1$ pair production is ~700 times larger than the LO cross section of the $\tilde{t}_1 t\tilde{\chi}^0_i$ production at $m_{\tilde{t}_1} = 200$ GeV. This ratio decreases for larger stop masses and becomes ~400 at $m_{\tilde{t}_1} = 600$ GeV. This is because for larger $m_{\tilde{t}_1}$ (and $m_{\tilde{\chi}^0_i}$), the relative importance of the top-quark mass decreases and the price to produce an extra top quark diminishes. The $\tilde{t}_1 t\tilde{\chi}^0_i$ production at lower stop masses has a comparable cross section with that of the Standard Model $t\bar{t}H$ process. The former is 105 fb at $m_{\tilde{t}_1} = 200$ GeV at LO, whereas the latter 508 fb [95] at NLO. This is not surprising because these processes share the same coupling due to supersymmetry.

III. THE MONOTOP SEARCH

A. The search strategy

In this section we study various kinematic distributions in the monotop channel and develop an optimal search strategy. We also derive the 2-σ sensitivity in the ($m_{\tilde{t}_1}$,$m_{\tilde{\chi}^0_1}$) plane assuming the high luminosity phase ($\int \mathcal{L}dt = 3$ ab^{-1}) of the 13 TeV LHC.

We begin by looking at the decay products of $\tilde{t}_1$ in the compressed stop-Higgsino region at parton level. The left panel of Fig. 4 shows the normalized transverse momentum distribution for b quarks p_{Tb} from the $\tilde{t}_1 \to b\tilde{\chi}^\pm_1$ decay. We display three distributions with $\Delta m_{\tilde{t}_1-\tilde{\chi}^0_1} = 8$, 15, and 45 GeV fixing $m_{\tilde{t}_1} = 317$ GeV and $m_{\tilde{\chi}^\pm_1} = m_{\tilde{\chi}^0_1} + 3$ GeV. Notice that for a small mass gaps, $\Delta m_{\tilde{t}_1-\tilde{\chi}^0_1} = 8$ and 15 GeV, almost all b quarks *do not* pass the $p_{Tb} > 30$ GeV cut, whereas for a larger mass difference, $\Delta m_{\tilde{t}_1-\tilde{\chi}^0_1} = 45$ GeV, a significant fraction of the b quarks *do* pass this selection.

The right panel of Fig. 4 shows the p_T distribution of a fermion (quark or lepton) from the $\tilde{\chi}^\pm_1 \to f\bar{f}'\tilde{\chi}^0_1$ decay. Different from the left panel, we now fix $\Delta m_{\tilde{t}_1-\tilde{\chi}^0_1} =$ 45 GeV and vary the mass difference between $\tilde{\chi}^\pm_1$ and $\tilde{\chi}^0_1$ as $\Delta m_{\tilde{\chi}^\pm_1-\tilde{\chi}^0_1} = 3$, 6, and 9 GeV.[5] We observe that p_{Tf} increases on average as $\Delta m_{\tilde{\chi}^\pm_1-\tilde{\chi}^0_1}$ increases. However, for $\Delta m_{\tilde{\chi}^\pm_1-\tilde{\chi}^0_1} \leq 9$ GeV the majority of the decay products are always very soft, $p_{Tf} < 10$ GeV. We have also checked that the p_{Tf} distribution is almost independent of $\Delta m_{\tilde{t}_1-\tilde{\chi}^0_1}$.

These distributions suggest that stop's decay products are soft in the compressed region and unlikely to pass the standard lepton and jet reconstruction criteria. In this case, all the visible objects in the final state arise from the top-quark decay (and QCD radiation) as illustrated in the right panel of Fig. 1. This monotop feature can be used to efficiently discriminate the signal from backgrounds.

We consider the monotop signature of the $\tilde{t}_1 t\tilde{\chi}^0_{1(2)}$ process with a leptonic top decay, by requiring exactly one isolated lepton ($\ell = e$ and μ) with $p_T > 10$ GeV [$N_\ell(p_T > 10\text{ GeV}) = 1$] and exactly one b-tagged jet with $p_T > 30$ GeV [$N_b(p_T > 30\text{ GeV}) = 1$]. To reduce the $t\bar{t}$ background, we also demand the number of jets with $p_T > 30$ GeV must be less than or equal to three.[6] Our baseline selection cut is thus summarized as

[5]In Natural SUSY scenarios the mass difference between $\tilde{\chi}^\pm_1$ and $\tilde{\chi}^0_1$ is smaller than 10 GeV if the electroweak gauginos are heavier than 1 TeV [96–98].

[6]Vetoing jets with a p_T much lower than the hard interaction scale may bring a large uncertainty proportional to a logarithm of the ratio of these two scales. For a study to understand and reduce this uncertainty, see [99].

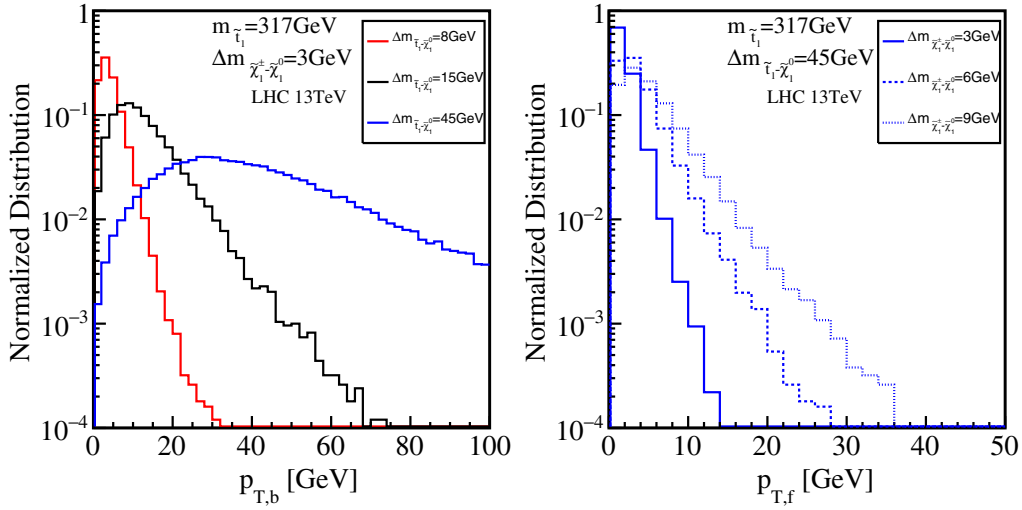

FIG. 4. Normalized transverse momentum distributions for the b quark from the $\tilde{t}_1 \to b\tilde{\chi}_1^\pm$ decay (left panel) and the fermions from the subsequent $\tilde{\chi}_1^\pm \to f\bar{f}'\tilde{\chi}_1^0$ decay (right panel) at parton level. In the left panel we fix the chargino-neutralino mass difference to $\Delta m_{\tilde{\chi}_1^\pm - \tilde{\chi}_1^0} = 3$ GeV and vary the stop-neutralino mass difference as $\Delta m_{\tilde{t}_1 - \tilde{\chi}_1^0} = 8$, 15, and 50 GeV, whereas on the right panel we fix $\Delta m_{\tilde{t}_1 - \tilde{\chi}_1^0} = 45$ GeV and scan $\Delta m_{\tilde{\chi}_1^\pm - \tilde{\chi}_1^0} = 3$, 6, and 9 GeV. We assume $m_{\tilde{t}_1} = 317$ GeV for both panels.

$$N_j(p_T > 30\ \text{GeV}) \leq 3,$$
$$N_b(p_T > 30\ \text{GeV}) = 1,$$
$$N_\ell(p_T > 10\ \text{GeV}) = 1. \tag{9}$$

After these selections, the main backgrounds come from $t\bar{t}$ (831 pb [100]), tW (71 pb [101]), tZ (0.88 pb [102]), and $W + b\bar{b}$ (7.65 pb), where the numbers in the brackets denote the production rate (before cuts) at Next-to-Next-to-Leading Order + Next-to-Next-to-Leading Log for $t\bar{t}$, at LO for $W + b\bar{b}$ and at NLO for all the other processes. The $t\bar{t}$ and $W + b\bar{b}$ samples are generated with ALPGEN [103] and Pythia 6 [104], and the $t\bar{t}$ sample is merged up to one jet in the MLM matching scheme. The signal and the other background samples are generated using MadGraph 5 [89] and showered and hadronized with Pythia 6.

The detector effects are included via the Delphes 3 package [105]. Jets are defined with the anti-k_T algorithm in Fastjet [106,107] with $R = 0.5$ and required $p_T > 20$ GeV and $|\eta| < 2.5$. We adopt the b-tagging efficiency of 70% with 15% mistag rate for c quarks and 1% for light quarks [108,109]. The isolated leptons are defined only within the range of $p_T > 10$ GeV and $|\eta| < 2.4$.

Using the detector-level samples after applying the baseline selection Eq. (9), we now show the distributions of the invariant mass of the b and ℓ ($\ell = e, \mu$) in the left panel of Fig. 5. As can be seen, the signal presents a Jacobian peak structure at $m_{b\ell} \sim 130$ GeV, and most of the signal events fall below 150 GeV. This structure is expected if the b and ℓ are originated from the same top-quark decay. Unlike the signal, the $m_{b\ell}$ distributions for $t\bar{t}$ and $W + b\bar{b}$ exhibit large tails exceeding 150 GeV. For $t\bar{t}$, this tail typically comes from the events where the b and ℓ come from different top-quark decays. For $W + b\bar{b}$, the Jacobian peak structure is not expected at the first place, since there is no top quark in the event. To exploit this feature we impose

$$m_{b\ell} < 150\ \text{GeV}. \tag{10}$$

Another variable that is useful to control the background is the transverse mass of the lepton and the missing energy vector: $m_T = \sqrt{2p_{T\ell}E_T^{\text{miss}}(1 - \cos\phi_{\ell,E_T^{\text{miss}}})}$. If the lepton and the missing energy are originated from a single W boson, this variable is kinematically bounded from above by m_W. This is the case for $W + b\bar{b}$ and the fraction of the $t\bar{t}$ events where one of the tops decays hadronically and the other leptonically $t\bar{t}_{1l}$ (including τ). The right panel of Fig. 5 shows the m_T distribution for the 13 TeV LHC with 3 ab^{-1} of data. As expected, the m_T distributions in the $W + b\bar{b}$ and $t\bar{t}_{1l}$ samples sharply drop above $m_T \sim m_W$. We require

$$m_T > 100\ \text{GeV} \tag{11}$$

to further suppress these backgrounds. Above this threshold the dominant backgrounds become $t\bar{t}$ and tW where all W s and tops decay leptonically (including τ), respectively denoted by $t\bar{t}_{2l}$ and tW_{2l}.

In Fig. 6, we display the missing energy distribution for the signal and background samples after imposing the above selection cuts Eqs. (9), (10), and (11). The E_T^{miss} distribution falls faster for the total background than for the signal. We exploit this fact by defining three signal regions

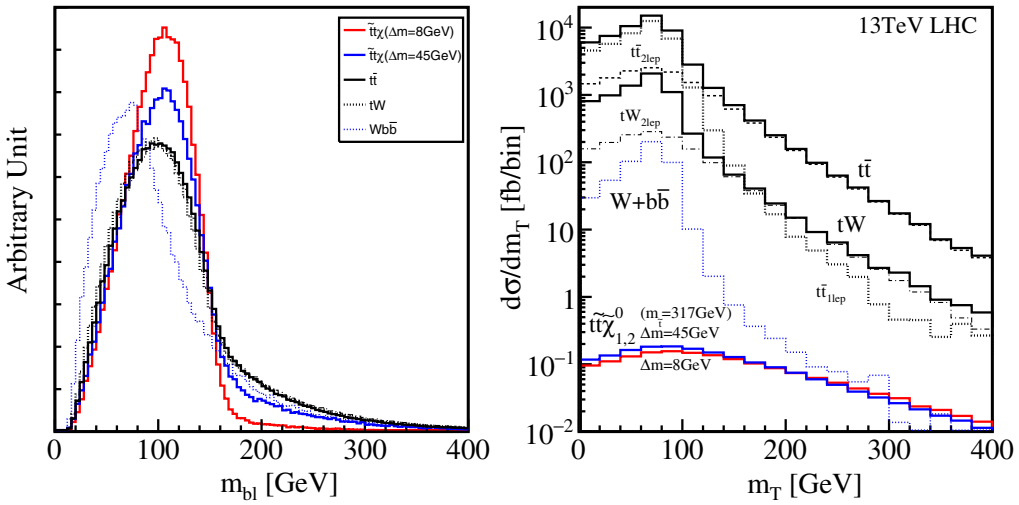

FIG. 5. Left: Normalized m_{bl} distributions for the signal $\tilde{t}_1 t\tilde{\chi}^0_{1(2)}$ with $\Delta m_{\tilde{t}_1-\tilde{\chi}^0_1} = 8$ GeV (red solid line) and 45 GeV (blue solid line), $t\bar{t}$ (black solid line), tW (black dotted line), and $W + b\bar{b}$ (blue dotted line) samples after the baseline selection. Right: Transverse mass m_T distributions after the baseline and $m_{b\ell} < 150$ GeV cuts expected at the 13 TeV LHC. The line types and colors are assigned in the same way as in the left panel apart from the tW, for which the black solid line is used. In this plot the contributions of the $t\bar{t}$ and tW where one or two W (and t) decay(s) leptonically (including τ) are also shown, which are $t\bar{t}_{2l}$ (black dashed line), $t\bar{t}_{1l}$ (black dotted line), and tW_{2l} (black dot-dashed line). For both plots the signal points have $m_{\tilde{t}_1} = 317$ GeV and $m_{\tilde{\chi}^\pm_1} = m_{\tilde{\chi}^0_2} = m_{\tilde{\chi}^0_1} + 3$ GeV.

(SR1, SR2, and SR3) that correspond to different missing energy selections

$$E_T^{\text{miss}}/\text{GeV} > 450(\text{SR1}), \qquad 500(\text{SR2}), \qquad 550(\text{SR3}). \tag{12}$$

A detailed cut-flow table showing the number of signal and background events at a high luminosity LHC with $\sqrt{s} = 13$ TeV and $\int \mathcal{L}dt = 3$ ab^{-1} is presented in Table I. Three benchmark points are examined for signal: $(m_{\tilde{t}_1}, m_{\tilde{\chi}^0_1})/\text{GeV} = (317, 309)$, (317, 272), and (342, 334), where the remaining parameters are fixed to $m_{\tilde{\chi}^\pm_1} = m_{\tilde{\chi}^0_2} = m_{\tilde{\chi}^0_1} + 3$ GeV, $\tan\beta = 20$, and $\cos\theta_{\tilde{t}} = 1$. The two numbers in the brackets displayed for signal in the last three columns are $S/\sqrt{B}$ and S/B, respectively. We assume that the higher order corrections to the signal are tantamount to a factor $K_{\text{NLO}} = 1.5$.[7] Notice that we can achieve with this analysis $S/\sqrt{B} \sim 2$–3 with $S/B \sim 0.1$–0.2 for $m_{\tilde{t}_1} \sim 310$–340 GeV.

B. The expected performance

We now compare the signal and background in the signal region and derive the 2-σ sensitivity at a high luminosity LHC with $\sqrt{s} = 13$ TeV and $\int \mathcal{L}dt = 3$ ab^{-1}. We present the sensitivity in a two-dimensional (2D) parameter plane $(m_{\tilde{t}_1}, m_{\tilde{\chi}^0_1})$ assuming $m_{\tilde{\chi}^\pm_1} = m_{\tilde{\chi}^0_2} = m_{\tilde{\chi}^0_1} + 3$ GeV and do not consider the contribution from $\tilde{t}_2$. We also consider two extreme cases: $\tilde{t}_1 = \tilde{t}_L$ and $\tilde{t}_1 = \tilde{t}_R$.

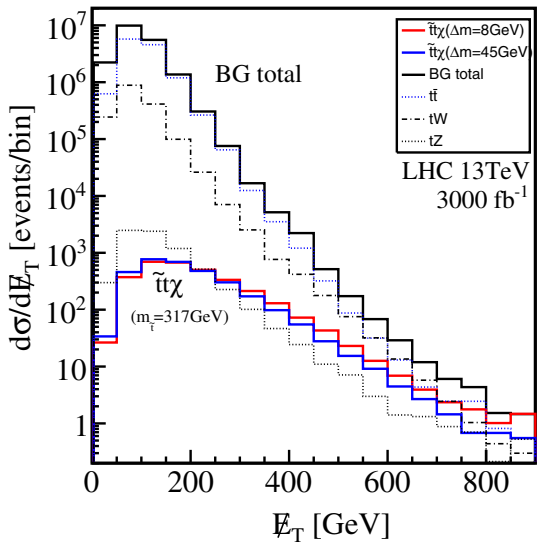

FIG. 6. Missing energy distribution E_T for the signal $\tilde{t}_1 t\tilde{\chi}^0_{1(2)}$ with $\Delta m_{\tilde{t}_1-\tilde{\chi}^0_1} = 8$ GeV (red solid line) and 45 GeV (blue solid line) and the total background (black solid line) after the selection cuts Eqs. (9), (10), and (11). The breakdowns of the total background are also shown: $t\bar{t}$ (blue dotted line), tW (black dash-dotted line), and tZ (black dotted line). The distributions are normalized to the number of expected events at the 13 TeV LHC with 3 ab^{-1} integrated luminosity. The signal points are assumed to have $m_{\tilde{t}_1} = 317$ GeV and $m_{\tilde{\chi}^\pm_1} = m_{\tilde{\chi}^0_2} = m_{\tilde{\chi}^0_1} + 3$ GeV. The last bin is an overflow bin.

[7]We notice that the literature does not provide higher order corrections to the considered signal process. As we consider all the main backgrounds at least at NLO and given the similarities between the signal and stop pair production, we assume a similar NLO K factor. We indicate, however, the importance of the precise NLO rate determination for future studies.

TABLE I. Number of signal and background events assuming a high luminosity LHC with $\sqrt{s} = 13$ TeV and $\int \mathcal{L}dt = 3$ ab^{-1}. We present results for three signal benchmark points: $(m_{\tilde{t}_1}, m_{\tilde{\chi}_1^0})/\text{GeV} = (317, 309)$, (317, 272), and (342, 334). The remaining parameters are fixed to $m_{\tilde{\chi}_1^\pm} = m_{\tilde{\chi}_2^0} = m_{\tilde{\chi}_1^0} + 3$ GeV, $\tan\beta = 20$, and $\cos\theta_{\tilde{t}} = 1$. We assume that the higher order corrections to the signal are tantamount to a factor $K_{\text{NLO}} = 1.5$.

Process	σ	Baseline	$m_{b\ell} < 150$	$m_T > 100$	SR1	SR2	SR3
$t\bar{t}$	831 pb	206×10^6	165×10^6	17.7×10^6	463.3	142.6	55.2
tW	71 pb	26.2×10^6	20.7×10^6	1.68×10^6	308.5	130.9	55.5
tZ	0.88 pb	22.8×10^3	21.6×10^3	7.3×10^3	26.1	15.1	8.0
$W + b\bar{b}$	7.65 pb	1.82×10^6	1.51×10^6	42.3×10^3	5.9	2.8	1.4
BG total	903 pb	226×10^6	41.1×10^6	19.4×10^6	803.8	291.4	120.1
BP(317, 309)	23.7 fb	5883	5491	3387	109 (3.8, 0.13)	61.4 (3.6, 0.21)	35.0 (3.2, 0.29)
BP(317, 272)	30.8 fb	6522	5491	3123	60.2 (2.1, 0.07)	34.9 (2.0, 0.12)	19.1 (1.7, 0.16)
BP(342, 334)	16.7 fb	4119	3834	2395	84.0 (3.0, 0.10)	46.8 (2.7, 0.16)	26.8 (2.4, 0.22)

We first display the LO cross section of the signal in the $(m_{\tilde{t}_1}, m_{\tilde{\chi}_1^0})$ plane in Fig. 7 for the $\tilde{t}_L$ (left panel) and $\tilde{t}_R$ (right panel) cases. In the calculation we take the pure Higgsino limit for the neutralino mixing and $\tan\beta = 20$, i.e. $\mathcal{R} \simeq 1$. One can see that the cross section decreases as either $m_{\tilde{t}_1}$ or $m_{\tilde{\chi}_1^0}$ increases. This is contrasted with the $\tilde{t}_1$ pair production, where the cross section depends only on $m_{\tilde{t}_1}$. As suggested in Eq. (8), the cross section is almost unchanged between the $\tilde{t}_L$ and $\tilde{t}_R$ cases.

We now look how the signal efficiency changes across the $(m_{\tilde{t}_1}, m_{\tilde{\chi}_1^0})$ plane. As an example, we display the signal efficiency of SR2 in Fig. 8 for the $\tilde{t}_L$ (left panel) and $\tilde{t}_R$ (right panel) cases. As can be seen, the efficiency varies from 0.08% to $\gtrsim$0.4% in the region of the plots. The efficiency is smaller for larger mass difference, $\Delta m_{\tilde{t}_1 - \tilde{\chi}_1^0}$. For larger $\Delta m_{\tilde{t}_1 - \tilde{\chi}_1^0}$ the b quark from the $\tilde{t}_1$ decay becomes harder and more visible, with which the event more likely fails to pass the $N_b = 1$ and $N_j \leq 3$ cuts. We also observe that the efficiency increases for larger $m_{\tilde{t}_1}$. Since the interaction scale is proportional to the mass of the system, the typical momentum scale of $\tilde{t}_1$, t, and $\tilde{\chi}_1^0$ becomes larger as $m_{\tilde{t}_1}$ increases. With those high p_T objects, events are more likely to pass the m_T and the missing energy cuts. The efficiencies are almost the same for the $\tilde{t}_L$ and $\tilde{t}_R$ cases. This suggests that our search strategy works independently of the details of the stop mixing.

We now show the 2-σ sensitivity expected at the 13 TeV LHC with $\int \mathcal{L}dt = 3$ ab^{-1} by the dark-, medium-, and light-pink regions in Fig. 9, corresponding to $\mathcal{R} = 0.5$, 0.75, and 1, respectively. The top and bottom panels are for

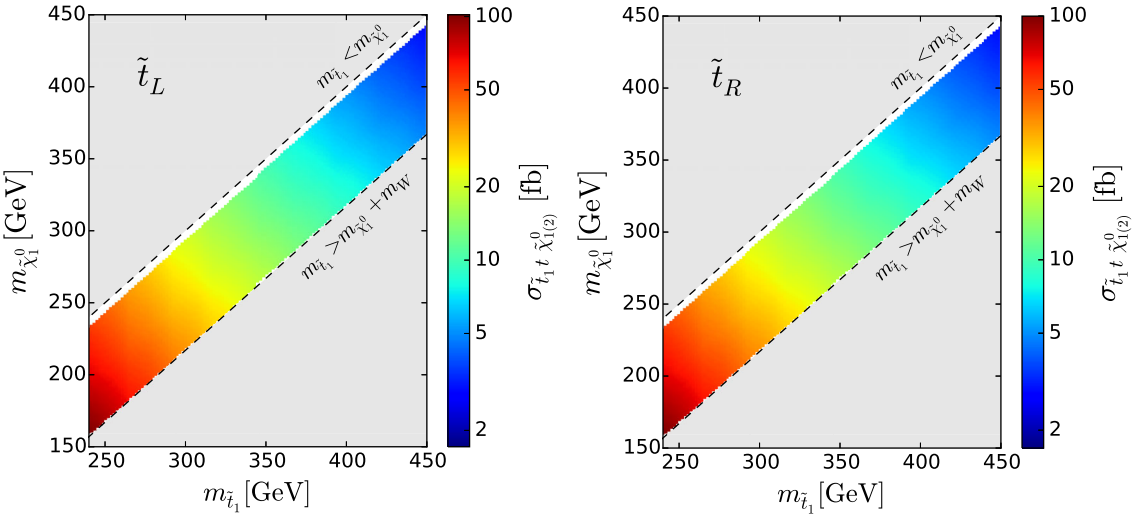

FIG. 7. The LO cross section in the $(m_{\tilde{t}_1}, m_{\tilde{\chi}_1^0})$ plane for the $\tilde{t}_1 = \tilde{t}_L$ (left) and $\tilde{t}_1 = \tilde{t}_R$ (right) cases.

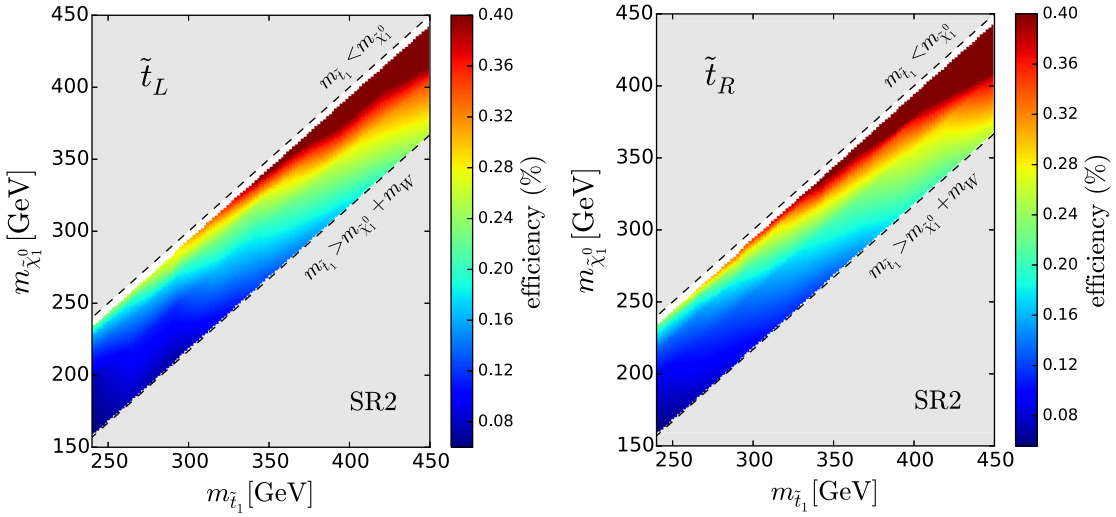

FIG. 8. The signal efficiency of SR2 in the $(m_{\tilde{t}_1}, m_{\tilde{\chi}_1^0})$ plane for the $\tilde{t}_1 = \tilde{t}_L$ (left) and $\tilde{t}_1 = \tilde{t}_R$ (right) cases.

the $\tilde{t}_L$ and $\tilde{t}_R$ cases. In deriving these sensitivities, only the signal regions with more than three expected signal events and $S/B > 0.1$ are used at each parameter point and $\mathcal{R}$. The latter condition is used to ensure that the effect of the systematic uncertainty is not too large. We then select the signal region that has the largest $S/\sqrt{B}$. The most sensitive signal region for each parameter point and $\mathcal{R}$ is given in the Appendix.

We also overlay the current 95% C.L. exclusion limit for the $\tilde{t}_1 \to b\chi_1^0$ topology with $m_{\tilde{\chi}_1^\pm} = m_{\tilde{\chi}_0^\pm}$ by grey regions. The region surrounded by the blue curve is the 95% C.L. excluded region by the ATLAS di-b-jet search [75] using early 13 TeV data with 3.2 fb^{-1}. ATLAS interprets their analysis in the $\tilde{b}_1$ production with $\tilde{b}_1 \to b\tilde{\chi}_1^0$ and derives the excluded region in the $(m_{\tilde{b}_1}, m_{\tilde{\chi}_1^0})$ plane. Since the production cross section and the decay kinematics are the same between this $\tilde{b}_1$ model and the $\tilde{t}_1$ pair production with $\tilde{t}_1 \to b\tilde{\chi}_1^\pm$ at $m_{\tilde{\chi}_1^\pm} = m_{\tilde{\chi}_1^0}$ and $m_{\tilde{t}_1} = m_{\tilde{b}_1}$, we simply use the $\tilde{b}_1$ excluded region for $\tilde{t}_1$ by identifying $m_{\tilde{t}_1} = m_{\tilde{b}_1}$. In realistic models with Higgsino-like $\tilde{\chi}_1^0$, $m_{\tilde{\chi}_1^\pm}$ is a few GeV larger than $m_{\tilde{\chi}_1^0}$. We therefore believe that the presented exclusion region in Fig. 9 is slightly aggressive in the compressed stop-Higgsino region since the b quark from $\tilde{t}_1 \to b\tilde{\chi}_1^\pm$ is softer compared to that from $\tilde{b}_1 \to b\tilde{\chi}_1^0$ at the same $m_{\tilde{\chi}_1^0}$ and $m_{\tilde{t}_1} = m_{\tilde{b}_1}$. The other two regions with dark and light green boundaries are the 95% C.L. excluded region by monojet searches by ATLAS [77] and CMS [74] based on Run 1 data.

One can see from Fig. 9 that the monotop search is sensitive for smaller $\Delta m_{\tilde{t}_1 - \tilde{\chi}_1^0}$. This is expected since the b jet from $\tilde{t}_1 \to b\tilde{\chi}_1^\pm$ becomes visible for larger $\Delta m_{\tilde{t}_1 - \tilde{\chi}_1^0}$, making the event difficult to pass the $N_b = 1$ and $N_j \leq 3$ cuts. The reach of the 2-σ sensitivity largely depends on the Higgsino measure, $\mathcal{R}$, to which the production cross section of the supersymmetric $t\bar{t}H$ process is proportional. Since the monojet search is only sensitive to the stop and neutralino masses, measuring both the monojet and the monotop signal rates enables us to directly probe the up-type Higgsino components in the neutralinos through $\mathcal{R}$. As can be seen, the sensitivity reaches up to $m_{\tilde{t}_1} \sim 375$ (340) (285) GeV for $\mathcal{R} = 1$ (0.75) (0.5) at the most compressed region. It is worth noting that these sensitivities are not superior to those from conventional monojet searches. For example, Ref. [110] shows that the 2-σ sensitivity of the monojet channel reaches up to $m_{\tilde{t}} \simeq m_{\tilde{\chi}_1^0} \sim 500$ GeV at the 14 TeV LHC with $\int \mathcal{L} dt = 3$ ab^{-1}. Nevertheless, the monotop channel is still very useful to probe the Higgsino components in the lightest neutralino as we have seen above. Additionally, this channel is also powerful to probe the L-R mixing of the stop sector as we will discuss in the next section.

We also observe that the 2-σ regions are almost identical between the $\tilde{t}_L$ and $\tilde{t}_R$ cases. This means the monotop search presented in this section works regardless of the details of the stop sector.

We finally comment on possible contributions from the $\tilde{t}_1$ pair production, which is not included in our calculation. The final state of this process is two b quarks from $\tilde{t}_1 \to b\tilde{\chi}_1^\pm$ and very soft fermions (possibly leptons) from $\tilde{\chi}_1^\pm \to f\bar{f}'\tilde{\chi}_1^0$. As shown in Fig. 4, the hardness of the b quarks varies depending on the mass gap between $\tilde{t}_1$ and $\tilde{\chi}_1^0$, whereas the leptons are always very soft as we fixed $\tilde{\chi}_1^\pm = \tilde{\chi}_1^0 + 3$ GeV. The missing energy is also tiny on average since the neutralinos are produced almost back to back in the transverse plane unless they are boosted recoiling against hard ISR jets. The efficiency of our event selection for the $\tilde{t}_1$ pair production is therefore extremely small. This very small efficiency can, however,

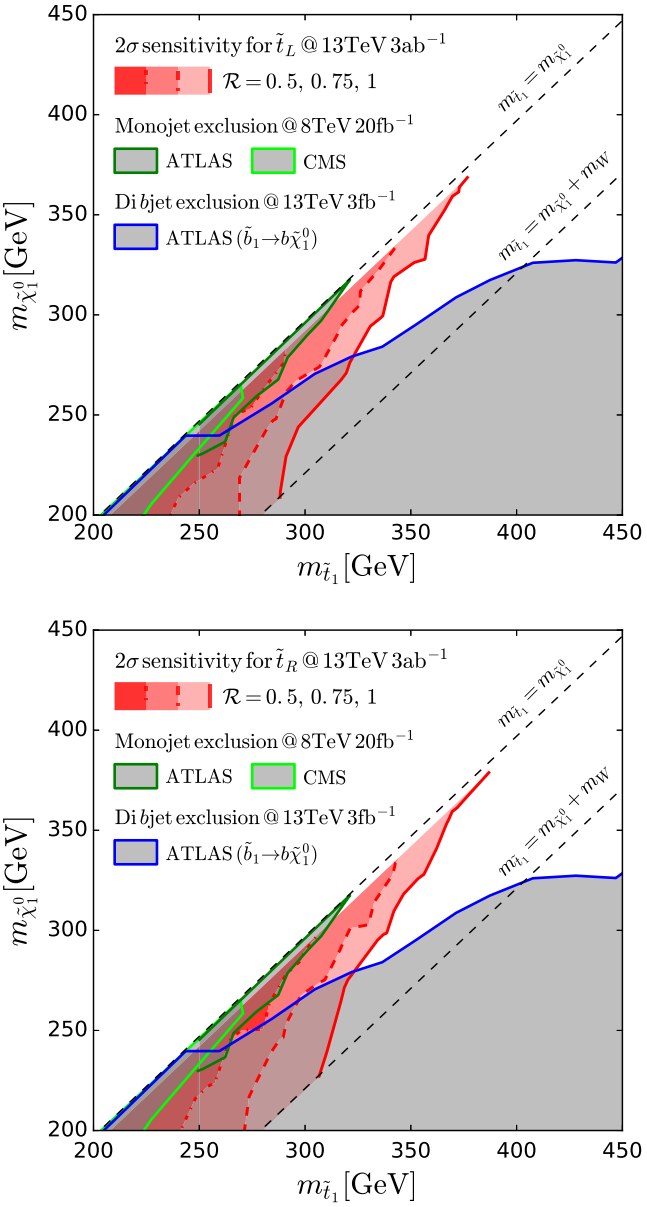

FIG. 9. The 2-σ sensitivities expected at the 13 TeV high luminosity LHC with $\int \mathcal{L}dt = 3$ ab^{-1} for $\mathcal{R} = 0.5$ (dark-pink region), 0.75 (medium-pink region), and 1 (light-pink region) for the $\tilde{t}_L$ (top) and $\tilde{t}_R$ (bottom) cases. In deriving these sensitivities, only the signal regions with more than three expected signal events and $S/B > 0.1$ are considered at each parameter point and $\mathcal{R}$. The signal region with the largest $S/\sqrt{B}$ is then used to derive the sensitivity. The current 95% C.L. excluded region is filled by grey. The region surrounded by the blue curve is obtained from the 13 TeV ATLAS di-b-jet analysis with $\int \mathcal{L}dt = 3.2$ fb^{-1} [75]. The regions with dark and light green boundaries are excluded by the ATLAS [77] and CMS [74] monojet searches with Run 1 data corresponding to $\int \mathcal{L}dt \simeq 20$ fb^{-1}.

be compensated to some extent by its considerably large production rate. We have checked numerically that the contribution from the $\tilde{t}_1$ pair production to our signal regions is about 30% of the $\tilde{t}_1 t\tilde{\chi}_{1(2)}^0$ contribution in the most compressed region and rises to ~70% in the moderately compressed region with $\Delta m_{\tilde{t}_1-\tilde{\chi}_1^0} \sim 50$ GeV. This suggests that the actual sensitivity of the monotop search is slightly better than what is shown in Fig. 9, making our results conservative. We leave the detailed study including the $\tilde{t}_1$ pair production to future analyses.

IV. PROBING THE STOP MIXING

We have seen that the monotop search presented in the previous section is insensitive to the stop mixing. The neutralino sector can be probed by measuring the signal rates of monojet and monotop channels without assuming the details of the stop sector. In this section we demonstrate, however, that kinematic distributions of the top-quark decay products are sensitive to the stop sector and can be used to measure the stop mixing [111,112].

At the vicinity of the pure Higgsino limit, the dominant contribution to the stop-top-neutralino interaction comes from

$$-\mathcal{L} \supset Y_t \Phi_{t_R} \Phi_{t_L^c} \Phi_{H_u^0}|_{\theta^2} \supset Y_t(\tilde{t}_R \bar{t}_L + t_R \tilde{t}_L^*)\tilde{H}_u^0 \supset Y_t(\cos\theta_{\tilde{t}} \bar{t}_L \tilde{t}_1 + \sin\theta_{\tilde{t}} t_R \tilde{t}_1^*) N_{i4} \tilde{\chi}_i^0, \quad (13)$$

where Φ_i is the chiral superfield of i and we have omitted the Hermitian conjugate terms. As can be seen, if $\tilde{t}_1$ is mostly $\tilde{t}_R$ ($\cos\theta_{\tilde{t}} \simeq 1$), the top quark tends to be left handed, and vice versa for $\tilde{t}_L$.

The chirality of the top-quark affects the kinematics of its decay products. For example, the angular distribution of the decay product $f(= b, \ell)$ is correlated with the top spin direction as [113–115]

$$\frac{1}{\Gamma_f}\frac{d\Gamma_f}{d\cos\theta_f} = \frac{1}{2}(1 + \omega_f P_t \cos\theta_f) \quad (14)$$

in the rest frame of the top quark, where θ_f is the angle between the decay product f and the top spin quantization axis, and P_t is the degree of the top polarization

$$P_t \equiv \frac{N(\uparrow) - N(\downarrow)}{N(\uparrow) + N(\downarrow)}. \quad (15)$$

For the top quark in the $pp \to \tilde{t}_1 t\tilde{\chi}_{1(2)}^0$ process we obtain $P_t \simeq \cos 2\theta_{\tilde{t}}$ in the pure Higgsino limit. The coefficient ω_f is given as $\omega_b = -0.41$ and $\omega_\ell = 1$ at tree level.

The fact that ω_b and ω_ℓ have different signs means that in the rest frame of the top quark their momentum vectors prefer to be in the opposite direction. If $\tilde{t}_1 = \tilde{t}_R$ ($\cos\theta_{\tilde{t}} = 1$), $P_t = 1$ meaning that the boost of the top quark is more likely to be in the direction of ℓ at the rest frame of the top. In this case, the lepton gets a positive boost on average, while the b quark gets a negative. For $\tilde{t}_1 = \tilde{t}_L$

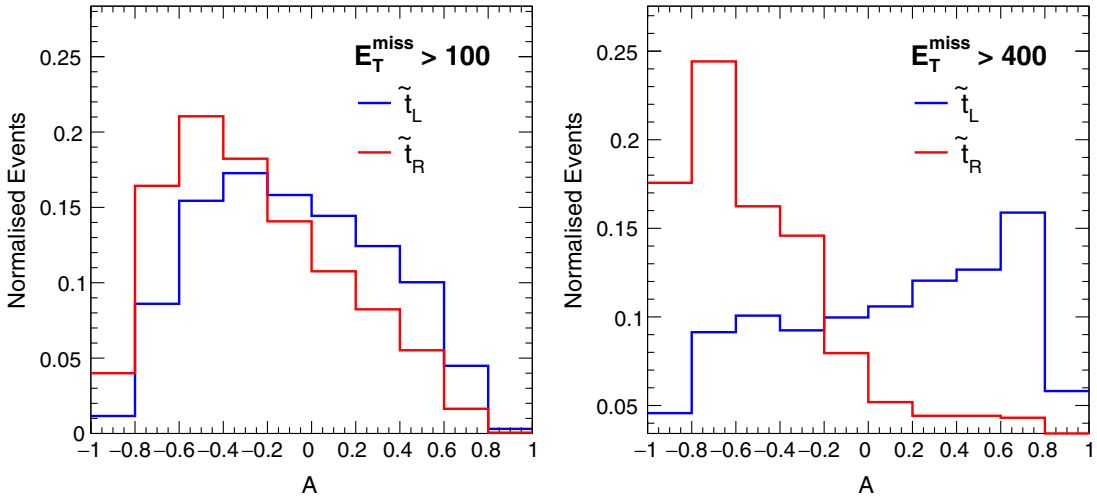

FIG. 10. The distribution of the p_T asymmetry, $\mathcal{A}$, at $(m_{\tilde{t}_1}, m_{\tilde{\chi}_1^0}) = (317, 309)$ GeV. The blue and red histograms correspond to the $\tilde{t}_1 = \tilde{t}_L$ and $\tilde{t}_1 = \tilde{t}_R$, respectively. The events satisfy the selection cuts described in Eqs. (9), (10), and (11). The events in the left and right plots additionally satisfy $E_T^{\text{miss}}/\text{GeV} > 100$ and 400, respectively.

$(\cos\theta_{\tilde{t}} = 0)$, the tendency is opposite. To capture this feature we define the p_T asymmetry, $\mathcal{A}$, as

$$\mathcal{A} \equiv \frac{p_T(\ell) - p_T(b)}{p_T(\ell) + p_T(b)}. \tag{16}$$

We display the distribution of $\mathcal{A}$ in Fig. 10 at $(m_{\tilde{t}_1}, m_{\tilde{\chi}_1^0}) = (317, 309)$ GeV for $\tilde{t}_1 = \tilde{t}_R$ (red line) and $\tilde{t}_1 = \tilde{t}_L$ (blue line). We only use the events that pass the selection cuts Eqs. (9), (10), (11), and $E_T^{\text{miss}}/\text{GeV} > 100$ (left panel) and 400 (right panel). As expected, the p_T asymmetry is larger (meaning that the lepton is more energetic) for $\tilde{t}_L$ compared to $\tilde{t}_R$. The tendency is drastically enhanced if the E_T^{miss} threshold is increased from 100 to 400 GeV, because the boost of the top quark increases. This demonstrates that the p_T asymmetry between the ℓ and b is a very useful variable to probe the stop mixing in the supersymmetric $t\bar{t}H$ process.

V. CONCLUSION

In this paper, we have studied the supersymmetric $t\bar{t}H$ process, i.e. $pp \to t\tilde{t}\,\tilde{h}$. We showed that a distinctive monotop signature arises from this channel for the Natural SUSY scenarios with small stop-Higgisino mass differences. While the current searches explore this compressed stop-Higgsino region with monojet channels exploiting the $\tilde{t}_1$ pair production associated with hard initial state radiation, our proposed channel serves complementary bounds granting a direct probe of the stop and neutralino sectors.

We presented a detailed search strategy to capture the supersymmetric $t\bar{t}H$ process and found that a high luminosity LHC at 13 TeV can probe the stop and Higgsino sectors if $m_{\tilde{t}_1} \lesssim 380$ GeV and $m_{\tilde{t}_1} - m_{\tilde{\chi}_1^0} \lesssim m_W$. We observed that this sensitivity increases for smaller mass differences $\Delta m_{\tilde{t}_1} - m_{\tilde{\chi}_1^0}$ and that our monotop search works regardless of the details of the stop sector.

Finally, we have demonstrated that the kinematic distributions of the top-quark decay products are sensitive to the stop sector and can be used to measure the stop mixing parameter. We proposed an asymmetry variable, $\mathcal{A}$, to access this parameter. Fortunately for our purposes, the performance of this observable dovetails nicely with the large missing energy selections required to reduce the background.

ACKNOWLEDGMENTS

D. G. and K. S. were supported by STFC through the IPPP grant. The work of M. T. was supported by World Premier International Research Center Initiative (WPI Initiative), MEXT, Japan.

APPENDIX: THE MOST SENSITIVE SIGNAL REGION

Figure 11 shows the most sensitive signal region (with the largest $S/\sqrt{B}$) for each parameter point and for $\mathcal{R} = 0.5$ (left panel), 0.75 (center panel), and 1 (right panel). The top and bottom panels correspond to the $\tilde{t}_1 = \tilde{t}_L$ and $\tilde{t}_1 = \tilde{t}_R$ cases, respectively. The empty circles represent the parameter points where none of the signal regions satisfies the sanity criteria that the signal contribution must be greater than three and $S/B > 0.1$.

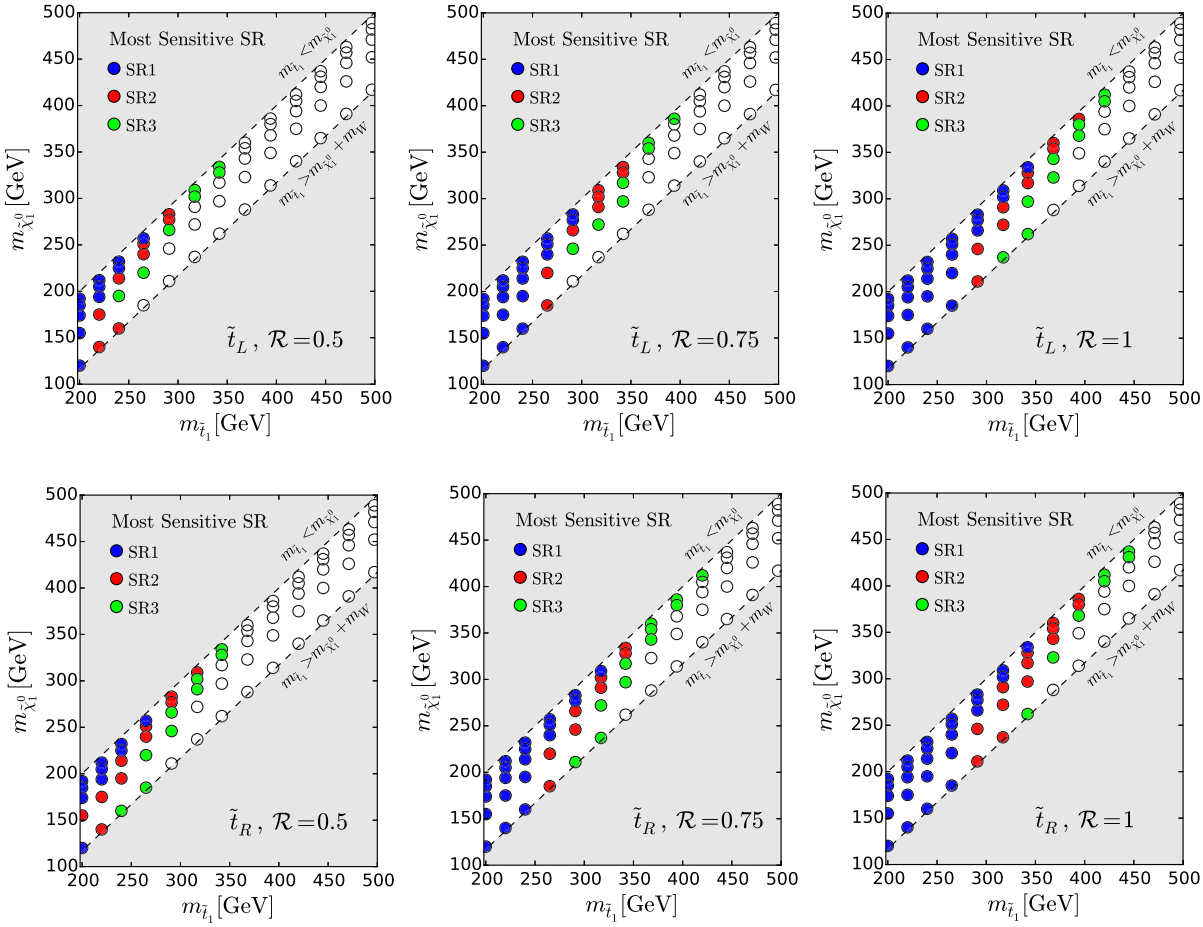

FIG. 11. The most sensitive signal region (with the largest $S/\sqrt{B}$) for each parameter point and for $\mathcal{R} = 0.5$ (left panel), 0.75 (center panel), and 1 (right panel). The top and bottom panels correspond to the $\tilde{t}_1 = \tilde{t}_L$ and $\tilde{t}_1 = \tilde{t}_R$ cases, respectively. The empty circles represent the parameter point where none of the signal regions satisfies the consistence criteria that the signal contribution must be greater than three and $S/B > 0.1$.

[1] G. Aad *et al.* (ATLAS Collaboration), Phys. Lett. B **749**, 519 (2015).
[2] G. Aad *et al.* (ATLAS Collaboration), Phys. Lett. B **740**, 222 (2015).
[3] V. Khachatryan *et al.* (CMS Collaboration), J. High Energy Phys. 09 (2014) 087; 10 (2014) 106(E).
[4] C. Degrande, J. M. Gérard, C. Grojean, F. Maltoni, and G. Servant, J. High Energy Phys. 07 (2012) 036; 03 (2013) 032(E).
[5] J. Ellis, D. S. Hwang, K. Sakurai, and M. Takeuchi, J. High Energy Phys. 04 (2014) 004.
[6] K. Nishiwaki, S. Niyogi, and A. Shivaji, J. High Energy Phys. 04 (2014) 011.
[7] S. Amor dos Santos *et al.*, Phys. Rev. D **92**, 034021 (2015).
[8] H.-L. Li, P.-C. Lu, Z.-G. Si, and Y. Wang, Chin. Phys. C **40**, 063102 (2016).
[9] N. Moretti, P. Petrov, S. Pozzorini, and M. Spannowsky, Phys. Rev. D **93**, 014019 (2016).
[10] M. R. Buckley and D. Goncalves, Phys. Rev. Lett. **116**, 091801 (2016).
[11] V. Khachatryan *et al.* (CMS Collaboration), J. High Energy Phys. 06 (2016) 177.
[12] F. Maltoni, K. Paul, T. Stelzer, and S. Willenbrock, Phys. Rev. D **64**, 094023 (2001).
[13] M. Farina, C. Grojean, F. Maltoni, E. Salvioni, and A. Thamm, J. High Energy Phys. 05 (2013) 022.
[14] C. Englert and E. Re, Phys. Rev. D **89**, 073020 (2014).
[15] A. Kobakhidze, L. Wu, and J. Yue, J. High Energy Phys. 10 (2014) 100.
[16] J. Yue, Phys. Lett. B **744**, 131 (2015).
[17] CERN Technical Report No. ATL-PHYS-PUB-2015-046, 2015, http://cds.cern.ch/record/2065974.

[18] CERN Technical Report No. CMS-PAS-FTR-15-002, 2015, https://cds.cern.ch/record/2063038.
[19] U. Baur, T. Plehn, and D. L. Rainwater, Phys. Rev. D **67**, 033003 (2003).
[20] M. J. Dolan, C. Englert, and M. Spannowsky, J. High Energy Phys. 10 (2012) 112.
[21] A. Papaefstathiou, L. L. Yang, and J. Zurita, Phys. Rev. D **87**, 011301 (2013).
[22] J. Baglio, A. Djouadi, R. Grober, M. M. Mühlleitner, J. Quevillon, and M. Spira, J. High Energy Phys. 04 (2013) 151.
[23] U. Baur, T. Plehn, and D. L. Rainwater, Phys. Rev. D **69**, 053004 (2004).
[24] M. J. Dolan, C. Englert, and M. Spannowsky, Phys. Rev. D **87**, 055002 (2013).
[25] F. Goertz, A. Papaefstathiou, L. L. Yang, and J. Zurita, J. High Energy Phys. 06 (2013) 016.
[26] D. Y. Shao, C. S. Li, H. T. Li, and J. Wang, J. High Energy Phys. 07 (2013) 169.
[27] M. Gouzevitch, A. Oliveira, J. Rojo, R. Rosenfeld, G. P. Salam, and V. Sanz, J. High Energy Phys. 07 (2013) 148.
[28] M. Papucci, J. T. Ruderman, and A. Weiler, J. High Energy Phys. 09 (2012) 035.
[29] L. J. Hall, D. Pinner, and J. T. Ruderman, J. High Energy Phys. 04 (2012) 131.
[30] N. Desai and B. Mukhopadhyaya, J. High Energy Phys. 05 (2012) 057.
[31] K. Ishiwata, N. Nagata, and N. Yokozaki, Phys. Lett. B **710**, 145 (2012).
[32] K. Sakurai and K. Takayama, J. High Energy Phys. 12 (2011) 063.
[33] S.-G. Kim, N. Maekawa, K. I. Nagao, M. M. Nojiri, and K. Sakurai, J. High Energy Phys. 10 (2009) 005.
[34] C. Wymant, Phys. Rev. D **86**, 115023 (2012).
[35] H. Baer, V. Barger, P. Huang, A. Mustafayev, and X. Tata, Phys. Rev. Lett. **109**, 161802 (2012).
[36] L. Randall and M. Reece, J. High Energy Phys. 08 (2013) 088.
[37] J. Cao, C. Han, L. Wu, J. M. Yang, and Y. Zhang, J. High Energy Phys. 11 (2012) 039.
[38] M. Asano and T. Higaki, Phys. Rev. D **86**, 035020 (2012).
[39] H. Baer, V. Barger, P. Huang, and X. Tata, J. High Energy Phys. 05 (2012) 109.
[40] J. A. Evans, Y. Kats, D. Shih, and M. J. Strassler, J. High Energy Phys. 07 (2014) 101.
[41] E. Hardy, J. High Energy Phys. 10 (2013) 133.
[42] G. D. Kribs, A. Martin, and A. Menon, Phys. Rev. D **88**, 035025 (2013).
[43] B. Bhattacherjee, J. L. Evans, M. Ibe, S. Matsumoto, and T. T. Yanagida, Phys. Rev. D **87**, 115002 (2013).
[44] K. Rolbiecki and K. Sakurai, J. High Energy Phys. 09 (2013) 004.
[45] D. Curtin, P. Meade, and P.-J. Tien, Phys. Rev. D **90**, 115012 (2014).
[46] J. S. Kim, K. Rolbiecki, K. Sakurai, and J. Tattersall, J. High Energy Phys. 12 (2014) 010.
[47] M. Papucci, K. Sakurai, A. Weiler, and L. Zeune, Eur. Phys. J. C **74**, 3163 (2014).
[48] J. A. Casas, J. M. Moreno, S. Robles, K. Rolbiecki, and B. Zaldvar, J. High Energy Phys. 06 (2015) 070.
[49] A. Katz, M. Reece, and A. Sajjad, J. High Energy Phys. 10 (2014) 102.
[50] B. Heidenreich and Y. Nakai, J. High Energy Phys. 10 (2014) 182.
[51] A. Mustafayev and X. Tata, Indian J. Phys. **88**, 991 (2014).
[52] F. Brümmer, S. Kraml, S. Kulkarni, and C. Smith, Eur. Phys. J. C **74**, 3059 (2014).
[53] T. Cohen, J. Kearney, and M. Luty, Phys. Rev. D **91**, 075004 (2015).
[54] K.-i. Hikasa, J. Li, L. Wu, and J. M. Yang, Phys. Rev. D **93**, 035003 (2016).
[55] D. Barducci, A. Belyaev, A. K. M. Bharucha, W. Porod, and V. Sanz, J. High Energy Phys. 07 (2015) 066.
[56] M. Drees and J. S. Kim, Phys. Rev. D **93**, 095005 (2016).
[57] L. Mitzka and W. Porod, arXiv:1603.06130.
[58] M. L. Graesser and J. Shelton, Phys. Rev. Lett. **111**, 121802 (2013).
[59] T. Plehn, M. Spannowsky, M. Takeuchi, and D. Zerwas, J. High Energy Phys. 10 (2010) 078.
[60] T. Plehn, M. Spannowsky, and M. Takeuchi, J. High Energy Phys. 05 (2011) 135.
[61] Z. Han, A. Katz, D. Krohn, and M. Reece, J. High Energy Phys. 08 (2012) 083.
[62] C. Kilic and B. Tweedie, J. High Energy Phys. 04 (2013) 110.
[63] D. S. M. Alves, M. R. Buckley, P. J. Fox, J. D. Lykken, and C.-T. Yu, Phys. Rev. D **87**, 035016 (2013).
[64] Y. Bai, H.-C. Cheng, J. Gallicchio, and J. Gu, J. High Energy Phys. 07 (2012) 110.
[65] M. R. Buckley, T. Plehn, and M. Takeuchi, J. High Energy Phys. 08 (2013) 086.
[66] Y. Bai, H.-C. Cheng, J. Gallicchio, and J. Gu, J. High Energy Phys. 08 (2013) 085.
[67] M. R. Buckley, T. Plehn, and M. J. Ramsey-Musolf, Phys. Rev. D **90**, 014046 (2014).
[68] M. Czakon, A. Mitov, M. Papucci, J. T. Ruderman, and A. Weiler, Phys. Rev. Lett. **113**, 201803 (2014).
[69] H. An and L.-T. Wang, Phys. Rev. Lett. **115**, 181602 (2015).
[70] A. Kobakhidze, N. Liu, L. Wu, J. M. Yang, and M. Zhang, Phys. Lett. B **755**, 76 (2016).
[71] S. Macaluso, M. Park, D. Shih, and B. Tweedie, J. High Energy Phys. 03 (2016) 151.
[72] H.-C. Cheng, C. Gao, L. Li, and N. A. Neill, J. High Energy Phys. 05 (2016) 036.
[73] G. Aad *et al.* (ATLAS Collaboration), J. High Energy Phys. 10 (2013) 189.
[74] V. Khachatryan *et al.* (CMS Collaboration), J. High Energy Phys. 06 (2015) 116.
[75] CERN Technical Report No. ATLAS-CONF-2015-066, 2015, https://cds.cern.ch/record/2114833.
[76] G. Aad *et al.* (ATLAS Collaboration), Phys. Rev. D **90**, 052008 (2014).
[77] M. Aaboud *et al.* (ATLAS Collaboration), Phys. Rev. D **94**, 032005 (2016).
[78] B. Fuks, P. Richardson, and A. Wilcock, Eur. Phys. J. C **75**, 308 (2015).
[79] G. Aad *et al.* (ATLAS Collaboration), Eur. Phys. J. C **75**, 79 (2015).

[80] V. Khachatryan *et al.* (CMS Collaboration), Phys. Rev. Lett. **114**, 101801 (2015).
[81] H. Davoudiasl, D. E. Morrissey, K. Sigurdson, and S. Tulin, Phys. Rev. D **84**, 096008 (2011).
[82] J. F. Kamenik and J. Zupan, Phys. Rev. D **84**, 111502 (2011).
[83] J. Andrea, B. Fuks, and F. Maltoni, Phys. Rev. D **84**, 074025 (2011).
[84] E. Alvarez, E. C. Leskow, J. Drobnak, and J. F. Kamenik, Phys. Rev. D **89**, 014016 (2014).
[85] J.-L. Agram, J. Andrea, M. Buttignol, E. Conte, and B. Fuks, Phys. Rev. D **89**, 014028 (2014).
[86] I. Boucheneb, G. Cacciapaglia, A. Deandrea, and B. Fuks, J. High Energy Phys. 01 (2015) 017.
[87] B. C. Allanach, S. Grab, and H. E. Haber, J. High Energy Phys. 01 (2011) 138; 09 (2011) 27.
[88] T. Binoth, D. Goncalves Netto, D. Lopez-Val, K. Mawatari, T. Plehn, and I. Wigmore, Phys. Rev. D **84**, 075005 (2011).
[89] J. Alwall, R. Frederix, S. Frixione, V. Hirschi, F. Maltoni, O. Mattelaer, H. S. Shao, T. Stelzer, P. Torrielli, and M. Zaro, J. High Energy Phys. 07 (2014) 079.
[90] W. Beenakker, M. Kramer, T. Plehn, M. Spira, and P. M. Zerwas, Nucl. Phys. **B515**, 3 (1998).
[91] W. Beenakker, S. Brensing, M. Kramer, A. Kulesza, E. Laenen, and I. Niessen, J. High Energy Phys. 08 (2010) 098.
[92] W. Beenakker, S. Brensing, M. Kramer, A. Kulesza, E. Laenen, L. Motyka, and I. Niessen, Int. J. Mod. Phys. A **26**, 2637 (2011).
[93] D. Goncalves, D. Lopez-Val, K. Mawatari, and T. Plehn, Phys. Rev. D **90**, 075007 (2014).
[94] W. Beenakker, C. Borschensky, M. Krämer, A. Kulesza, E. Laenen, S. Marzani, and J. Rojo, Eur. Phys. J. C **76**, 53 (2016).
[95] LHC Higgs Cross Section Working Group, https://twiki.cern.ch/twiki/bin/view/LHCPhysics/LHCHXSWG.
[96] N. E. Bomark, A. Kvellestad, S. Lola, P. Osland, and A. R. Raklev, J. High Energy Phys. 05 (2014) 007.
[97] C. Han, D. Kim, S. Munir, and M. Park, J. High Energy Phys. 04 (2015) 132.
[98] M. Badziak, A. Delgado, M. Olechowski, S. Pokorski, and K. Sakurai, J. High Energy Phys. 11 (2015) 053.
[99] F. J. Tackmann, W. J. Waalewijn, and L. Zeune, J. High Energy Phys. 07 (2016) 119.
[100] M. Czakon, P. Fiedler, and A. Mitov, Phys. Rev. Lett. **110**, 252004 (2013).
[101] LHC Top Working Group, https://twiki.cern.ch/twiki/bin/view/LHCPhysics/SingleTopRefXsec.
[102] J. Campbell, R. K. Ellis, and R. Röntsch, Phys. Rev. D **87**, 114006 (2013).
[103] M. L. Mangano, M. Moretti, F. Piccinini, R. Pittau, and A. D. Polosa, J. High Energy Phys. 07 (2003) 001.
[104] T. Sjostrand, S. Mrenna, and P. Z. Skands, Comput. Phys. Commun. **178**, 852 (2008).
[105] S. Ovyn, X. Rouby, and V. Lemaitre, arXiv:0903.2225.
[106] M. Cacciari, G. P. Salam, and G. Soyez, J. High Energy Phys. 04 (2008) 063.
[107] M. Cacciari, G. P. Salam, and G. Soyez, Eur. Phys. J. C **72**, 1896 (2012).
[108] CMS Collaboration, Report No. CMS-PAS-BTV-13-001, (2013).
[109] D. Goncalves, F. Krauss, and R. Linten, Phys. Rev. D **93**, 053013 (2016).
[110] M. Low and L.-T. Wang, J. High Energy Phys. 08 (2014) 161.
[111] B. Bhattacherjee, S. K. Mandal, and M. Nojiri, J. High Energy Phys. 03 (2013) 105.
[112] A. Papaefstathiou and K. Sakurai, J. High Energy Phys. 06 (2012) 069.
[113] M. Jezabek, Nucl. Phys. B, Proc. Suppl. **37B**, 197 (1994).
[114] A. Brandenburg, Z. G. Si, and P. Uwer, Phys. Lett. B **539**, 235 (2002).
[115] R. M. Godbole, K. Rao, S. D. Rindani, and R. K. Singh, J. High Energy Phys. 11 (2010) 144.